Karlsruher Institut für Technologie
Institut für Baustatik

A coupled two–scale shell model with applications to layered structures

F. Gruttmann, W. Wagner

Mitteilung 3(2012)

Karlsruher Institut für Technologie
Institut für Baustatik

A coupled two–scale shell model with applications to layered structures

F. Gruttmann, W. Wagner

Mitteilung 3(2012)

Prof. Dr.–Ing. W. Wagner
Institut für Baustatik
Karlsruher Institut für Technologie
Kaiserstr. 12
76131 Karlsruhe

Telefon: +49 721 608 42280
Telefax: +49 721 608 46015
E–mail: info@ibs.kit.edu
Internet: http://www.ibs.kit.edu

A coupled two–scale shell model with applications to layered structures

F. Gruttmann

Fachgebiet Festkörpermechanik
Technische Universität Darmstadt
Petersenstr. 13
64287 Darmstadt
Germany

W. Wagner

Institut für Baustatik
Karlsruher Institut für Technologie
Kaiserstraße 12
76131 Karlsruhe
Germany

Contents

Summary In this paper a coupled two–scale shell model is presented. A variational formulation and associated linearization for the coupled global–local boundary value problem is derived. For small strain problems various numerical solutions are computed within the so–called FE^2 method. The discretization of the shell is performed with quadrilaterals whereas the local boundary value problems at the integration points of the shell are discretized using 8–noded or 27–noded brick elements or so-called solid shell elements. At the bottom and top surface of the representative volume element stress boundary conditions are applied, whereas at the lateral surfaces the inplane displacements are prescribed. For the out of plane displacements link conditions are applied. The coupled nonlinear boundary value problems are simultaneously solved within a Newton iteration scheme. With an important test the correct material matrix for the stress resultants assuming linear elasticity and a homogeneous continuum is verified.

1 Introduction

Finite shell elements which are based on the first–order shear deformation theory are able to describe the global deformation behaviour of thin plate and shell structures. However for some stress components only an average shape through the thickness can be obtained. Various methods have been developed to obtain the complicated local deformation behaviour in inhomogeneous thin structures. In this context the authors in [1] discuss different models for the computation of stress concentrations in layered shells.
So–called multi–director shell formulations with an appropriate number of global degrees of freedom at the nodes yield approximate solutions of the three–dimensional boundary value problem, e.g. [2]. To reduce the effort the domains with multi–director discretization are adaptively coupled with 5 parameter shell elements in [3]. The coupling is accomplished in such a way that perturbations of the stress field are avoided. The application of brick elements or solid shell elements provides likewise a computationally expensive approach, e.g. [4, 5]. For laminates each layer must be discretized with several elements in thickness direction to obtain satisfactory results. The numerical effort for such a full–scale solution leads for practical problems to an unreasonable number of unknowns.
To avoid large-scale computations, the shells are treated as a homogeneous continuum with effective properties obtained through a homogenization procedure. The homogenization of laminated shells considering different composite theories is described e.g. in the textbook [2]. Sandwich panels consist of a heterogeneous core bonded to the face sheets. Effective properties of the core can first be determined applying analytical or numerical homogenization methods for a three-dimensional continuum. Hence the whole sandwich structure can be analyzed by application of a laminate theory, see e.g. [6, 7, 8].
The homogenization of masonry structures considering a particular stacking and material behaviour of the constituents has been treated e.g. in [9, 10, 11, 12, 13].
Computational homogenization procedures for thin structured sheets have been proposed in [14, 15]. The theory in [14] is based on a Reissner–Mindlin kinematic, whereas in [15] a Kirchhoff-Love kinematic is adopted. Representative volume elements (RVE) extending through the full thickness of the structure are introduced. At the top and bottom surfaces of the RVE stress boundary conditions are applied, whereas periodicity constraints are applied at the lateral surfaces. Numerical multiscale modeling of sandwich plates is performed in [16]. The authors consider a Reissner–Mindlin plate theory with five degrees of freedom on the macroscale, and three dimensional boundary value problems are solved on the mesoscale resolving the stacking order of the sandwich.

A lot of literature exists on computational homogenization methods for general heterogeneous materials, see e.g. [17, 18] for a survey and new developments. Solutions of two coupled boundary value problems, one on the macro scale and one on the micro scale, are computed. Arbitrary material behaviour on the micro level including physical and geometrical evolution of the microstructure can be considered. The macroscopic stresses and moduli are obtained with the solution of the associated microscale boundary value problem, e.g. [19, 20, 21, 22, 23, 24, 25, 26, 27, 28, 29] among many others. Computational homogenization methods are well suited for parallelization. The computing time to set up the global stiffness matrix is practically scaled by the number of processors.

The essential features and new aspects of the present formulation are summarized as follows:

(i) The underlying shell formulation is based on the Reissner–Mindlin theory with inextensible director field which leads to averaged transverse shear strains and vanishing thickness normal strains. The total displacement field is split in an average part introduced in the shell theory and a fluctuation part which describes warping and thickness change. A variational formulation and associated linearization for the coupled global–local boundary value problem is derived.

(ii) For the solution of the two–scale problem a FE^2 method for small strains is described, see Fig. 1. The reference surface of the shell structure is discretized using quadrilateral elements and the discretization of the local boundary value problems is performed with 8-noded or 27–noded brick elements and so-called solid shell elements. The RVE extends through the total thickness of the shell. At the lower and upper surface of the RVE stress boundary conditions are considered, whereas at the lateral surfaces the in–plane displacements are prescribed. The out of plane displacements of two opposite surfaces are linked in such a way that particular membrane, bending and shear modes are not restrained.

(iii) The nonlinear coupled local and global boundary value problems are simultaneously solved in a Newton iteration scheme, which is more effective than a nested iteration. Examples show that quadratic convergence of Newton´s method is preserved.

(iv) For a homogeneous shell and linear elasticity the material matrix for the stress resultants must be decoupled with respect to the submatrices for membrane, bending and shear. This important test is performed by means a homogeneous RVE. The finite element results for the submatrices are compared with the elementary analytical solution. The examples show that the developed two–scale model is able to analyze the mechanical behaviour of heterogeneous shell structures.

2 Variational formulation of the two–scale problem

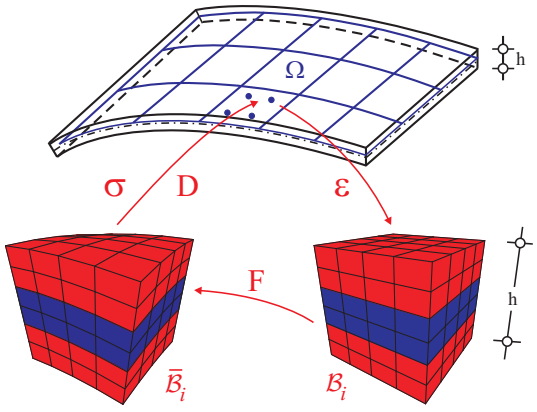

Figure 1: Computational homogenization of a layered shell

Let $\mathcal{B}$ be the three–dimensional Euclidean space occupied by a shell with thickness h in the reference configuration. With ξ^i we denote a convected coordinate system of the body. The

thickness coordinate $\xi^3 = z$ is defined in the range $h^- \leq z \leq h^+$, where h^- and h^+ are the $z-$coordinates of the outer surfaces. Thus, an arbitrary reference surface Ω with boundary Γ is introduced. The coordinate on $\Gamma = \Gamma_\sigma \bigcup \Gamma_u$ is denoted by S. The shell is loaded statically by loads $\bar{\mathbf{p}}$ in Ω and by boundary forces $\bar{\mathbf{t}}$ on Γ_σ. The part of the boundary with prescribed displacements or rotations is denoted by Γ_u. In the following Greek indices range from 1 to 2 and commas denote partial differentiation with respect to ξ^α.
Position vectors of the initial reference surface and current surface are denoted by $\mathbf{X}(\xi^\alpha)$ and $\mathbf{x}(\xi^\alpha)$, respectively. Furthermore, a director $\bar{\mathbf{D}}(\xi^\alpha)$ with $|\bar{\mathbf{D}}(\xi^\alpha)| = 1$ is introduced as a vector field perpendicular to Ω. The unit director field $\bar{\mathbf{d}}(\xi^\alpha)$ of the current configuration is obtained by orthogonal transformations and is a function of the rotational parameters $\bar{\boldsymbol{\omega}}$. Within the Reissner–Mindlin theory transverse shear strains are accounted for, thus $\bar{\mathbf{d}} \cdot \mathbf{x}_{,\alpha} \neq 0$.
Hence, the displacement field follows from the difference of the position vectors in shell space

$$\bar{\mathbf{u}} = \bar{\mathbf{u}}_0 + z\,(\bar{\mathbf{d}} - \bar{\mathbf{D}}) \qquad\qquad \bar{\mathbf{u}}_0 = \mathbf{x} - \mathbf{X}\,. \tag{1}$$

The shell strains are derived from the Green–Lagrangian strain tensor using kinematic assumption (1) and are arranged in a vector as

$$\boldsymbol{\varepsilon}(\bar{\mathbf{u}}_0, \bar{\boldsymbol{\omega}}) = [\varepsilon_{11}, \varepsilon_{22}, 2\,\varepsilon_{12}, \kappa_{11}, \kappa_{22}, 2\,\kappa_{12}, \gamma_1, \gamma_2]^T\,. \tag{2}$$

The components are membrane strains $\varepsilon_{\alpha\beta}$, curvatures $\kappa_{\alpha\beta}$ and transverse shear strains γ_α

$$\begin{aligned} \varepsilon_{\alpha\beta} &= \frac{1}{2}(\mathbf{x}_{,\alpha}\cdot\mathbf{x}_{,\beta} - \mathbf{X}_{,\alpha}\cdot\mathbf{X}_{,\beta}) \\ \kappa_{\alpha\beta} &= \frac{1}{2}(\mathbf{x}_{,\alpha}\cdot\bar{\mathbf{d}}_{,\beta} + \mathbf{x}_{,\beta}\cdot\bar{\mathbf{d}}_{,\alpha} - \mathbf{X}_{,\alpha}\cdot\bar{\mathbf{D}}_{,\beta} - \mathbf{X}_{,\beta}\cdot\bar{\mathbf{D}}_{,\alpha}) \\ \gamma_\alpha &= \mathbf{x}_{,\alpha}\cdot\bar{\mathbf{d}} - \mathbf{X}_{,\alpha}\cdot\bar{\mathbf{D}}\,. \end{aligned} \tag{3}$$

The normal strains in thickness direction are zero due to the assumed inextensible director field.

According to Fig. 1 a representative volume element (RVE) at an integration point i of a typical finite shell element is introduced. The domain $\mathcal{B}_i$ extends through the total thickness h of the shell. The displacement field is split in an averaged part $\bar{\mathbf{u}}$ and a fluctuation part $\tilde{\mathbf{u}}$.

$$\mathbf{u} = \bar{\mathbf{u}} + \tilde{\mathbf{u}} \tag{4}$$

The averaged displacements $\bar{\mathbf{u}}$ according to (1) are a linear function of the thickness coordinate, whereas $\tilde{\mathbf{u}}$ describes warping and thickness change. Hence, the deformation gradient $\mathbf{F} = \mathbf{1} + \operatorname{Grad}\mathbf{u}$ is defined in a standard way and the Green–Lagrangian strain tensor follows from $\mathbf{E} = \frac{1}{2}(\mathbf{F}^T\mathbf{F} - \mathbf{1})$.
Next the static field equations of the global and local boundary value problems are summarized. Therefore, we first introduce the vector of stress resultants and of the stress couple resultants

$$\mathbf{n}^\alpha = \int_{h^-}^{h^+} \mathbf{P}\,\mathbf{G}^\alpha \bar{\mu}\,dz \qquad\qquad \mathbf{m}^\alpha = \bar{\mathbf{d}} \times \int_{h^-}^{h^+} \mathbf{P}\,\mathbf{G}^\alpha z\bar{\mu}\,dz\,, \tag{5}$$

which are integrals of the First Piola–Kirchhoff stress tensor $\mathbf{P}$. Furthermore $\mathbf{G}^\alpha$ are contravariant base vectors and $\bar{\mu}$ is defined with the volume element $dV = \bar{\mu}\,dz\,dA$ and the

area element $dA = j\, d\xi^1\, d\xi^2$ with $j = |\mathbf{X}_{,1} \times \mathbf{X}_{,2}|$ of the reference surface. For a rectangular domain $\mathcal{B}_i$ as is depicted in Fig. 1 $\bar{\mu} = 1$ holds. The first two equations

$$\begin{aligned} \frac{1}{j}\,(j\,\mathbf{n}^\alpha)_{,\alpha} + \bar{\mathbf{p}} &= \mathbf{0}\,, \qquad \frac{1}{j}\,(j\,\mathbf{m}^\alpha)_{,\alpha} + \mathbf{x}_{,\alpha} \times \mathbf{n}^\alpha = \mathbf{0} \qquad \text{in } \Omega \\ \operatorname{Div} \mathbf{P} + \rho_0\,\mathbf{b} &= \mathbf{0} \qquad \text{in } \mathcal{B}_i\,. \end{aligned} \tag{6}$$

in (6) describe the global equilibrium, whereas the third equation is associated with the local equilibrium. The volume forces $\rho_0\,\mathbf{b}$ are neglected in the following. To complete the boundary value problem we specify the static boundary conditions of the reference surface

$$j\,(\mathbf{n}^\alpha\,\nu_\alpha) - \bar{\mathbf{t}} = \mathbf{0} \qquad j\,(\mathbf{m}^\alpha\,\nu_\alpha) = \mathbf{0} \quad \text{on} \quad \Gamma_\sigma\,, \tag{7}$$

where ν_α are components of the outward normal vector on Γ. The lower surface of the shell $\partial\mathcal{B}_i^-$ and the upper surface $\partial\mathcal{B}_i^+$ are free of stresses, thus

$$(\mathbf{P}\,\mathbf{N})_{z=h^-} = \mathbf{0} \quad \text{on} \quad \partial\mathcal{B}_i^- \qquad\qquad (\mathbf{P}\,\mathbf{N})_{z=h^+} = \mathbf{0} \quad \text{on} \quad \partial\mathcal{B}_i^+\,, \tag{8}$$

where $\mathbf{N}$ is the normal vector on $\partial\mathcal{B}_i$ at $z = h^-$ and $z = h^+$.

The weak form of the equilibrium equations (6) is now written with $\mathbf{v} = [\bar{\mathbf{u}}_0, \bar{\boldsymbol{\omega}}, \mathbf{u}]^T$ and admissible variations $\delta\mathbf{v} = [\delta\bar{\mathbf{u}}_0, \delta\bar{\boldsymbol{\omega}}, \delta\mathbf{u}]^T$

$$\begin{aligned} g(\mathbf{v}, \delta\mathbf{v}) = \; & - \int_\Omega [(\frac{1}{j}\,(j\,\mathbf{n}^\alpha)_{,\alpha} + \bar{\mathbf{p}}) \cdot \delta\bar{\mathbf{u}}_0 + (\frac{1}{j}\,(j\,\mathbf{m}^\alpha)_{,\alpha} + \mathbf{x}_{,\alpha} \times \mathbf{n}^\alpha) \cdot \delta\bar{\boldsymbol{\omega}}]\, dA \\ & - \sum_{e=1}^{numel} \sum_{i=1}^{NGP} \frac{1}{A_i} \int_{\Omega_i} \int_{h^-}^{h^+} \operatorname{Div} \mathbf{P} \cdot \delta\mathbf{u}\; \bar{\mu}\, dz\, dA = 0\,. \end{aligned} \tag{9}$$

Here, *numel* denotes the total number of shell elements, *NGP* the number of Gauss points for each element and $A_i = l_x\, l_y$ is the reference area of the RVE, see section 4. In case of an adaptive computation *numel* is the number of elements with two-scale modeling.
By default, the two integrals in (9) are integrated by parts. First, using

$$\begin{aligned} \mathbf{n}^\alpha &= n^{\alpha\beta}\,\mathbf{x}_{,\beta} + q^\alpha \bar{\mathbf{d}} + m^{\alpha\beta}\,\bar{\mathbf{d}}_{,\beta} \\ \mathbf{m}^\alpha &= \bar{\mathbf{d}} \times m^{\alpha\beta}\,\mathbf{x}_{,\beta} \end{aligned} \tag{10}$$

where the summation convention for repeated indices is used, integration by parts of the first integral yields with boundary conditions (7)

$$\begin{aligned} & - \int_\Omega [(\frac{1}{j}\,(j\,\mathbf{n}^\alpha)_{,\alpha} + \bar{\mathbf{p}}) \cdot \delta\bar{\mathbf{u}}_0 + (\frac{1}{j}\,(j\,\mathbf{m}^\alpha)_{,\alpha} + \mathbf{x}_{,\alpha} \times \mathbf{n}^\alpha) \cdot \delta\bar{\boldsymbol{\omega}}]\, dA \\ & = \int_\Omega (\boldsymbol{\sigma} \cdot \delta\boldsymbol{\varepsilon} - \bar{\mathbf{p}} \cdot \delta\bar{\mathbf{u}}_0)\, dA - \int_{\Gamma_\sigma} [j(\mathbf{n}^\alpha \nu_\alpha) \cdot \delta\bar{\mathbf{u}}_0 + j(\mathbf{m}^\alpha \nu_\alpha) \cdot \delta\bar{\boldsymbol{\omega}}]\, dS \\ & = \int_\Omega (\boldsymbol{\sigma} \cdot \delta\boldsymbol{\varepsilon} - \bar{\mathbf{p}} \cdot \delta\bar{\mathbf{u}}_0)\, dA - \int_{\Gamma_\sigma} \bar{\mathbf{t}} \cdot \delta\bar{\mathbf{u}}_0\, dS\,. \end{aligned} \tag{11}$$

Here, $\boldsymbol{\sigma}$ denotes the vector of stress resultants

$$\boldsymbol{\sigma} = [n^{11}, n^{22}, n^{12}, m^{11}, m^{22}, m^{12}, q^1, q^2]^T \tag{12}$$

with membrane forces $n^{\alpha\beta} = n^{\beta\alpha}$, bending moments $m^{\alpha\beta} = m^{\beta\alpha}$ and shear forces q^α. The so–called effective stress resultants $n^{\alpha\beta}$, $m^{\alpha\beta}$ and q^α enter in $\mathbf{n}^\alpha$ and $\mathbf{m}^\alpha$ according to (10). The virtual shell strains follow from (3) and read $\delta\boldsymbol{\varepsilon} = [\delta\varepsilon_{11}, \delta\varepsilon_{22}, 2\delta\varepsilon_{12}, \delta\kappa_{11}, \delta\kappa_{22}, 2\delta\kappa_{12}, \delta\gamma_1, \delta\gamma_2]^T$

$$\begin{aligned} \delta\varepsilon_{\alpha\beta} &= \frac{1}{2}(\delta\mathbf{x}_{,\alpha}\cdot\mathbf{x}_{,\beta} + \delta\mathbf{x}_{,\beta}\cdot\mathbf{x}_{,\alpha}) \\ \delta\kappa_{\alpha\beta} &= \frac{1}{2}(\delta\mathbf{x}_{,\alpha}\cdot\bar{\mathbf{d}}_{,\beta} + \delta\mathbf{x}_{,\beta}\cdot\bar{\mathbf{d}}_{,\alpha} + \delta\bar{\mathbf{d}}_{,\alpha}\cdot\mathbf{x}_{,\beta} + \delta\bar{\mathbf{d}}_{,\beta}\cdot\mathbf{x}_{,\alpha}) \\ \delta\gamma_\alpha &= \delta\mathbf{x}_{,\alpha}\cdot\bar{\mathbf{d}} + \delta\bar{\mathbf{d}}\cdot\mathbf{x}_{,\alpha}\ . \end{aligned} \tag{13}$$

Hence, applying the divergence theorem to the second integral considering boundary conditions (8) yields

$$-\int_{\Omega_i}\int_{h^-}^{h^+} \mathrm{Div}\,\mathbf{P}\cdot\delta\mathbf{u}\;\bar{\mu}\;dz\;dA = \int_{\Omega_i}\int_{h^-}^{h^+} \mathbf{S}:\delta\mathbf{E}\;\bar{\mu}\;dz\;dA\,. \tag{14}$$

Here, $\mathbf{S}$ denotes the Second Piola-Kirchhoff stress tensor with $\mathbf{P} = \mathbf{F}\,\mathbf{S}$ and the virtual Green-Lagrangian strain tensor $\delta\mathbf{E} = \frac{1}{2}(\delta\mathbf{F}^T\mathbf{F} + \mathbf{F}^T\delta\mathbf{F})$. Inserting (11) and (14) in eq. (9) yields

$$\begin{aligned} g(\mathbf{v},\delta\mathbf{v}) &= \int_{(\Omega)} (\boldsymbol{\sigma}\cdot\delta\boldsymbol{\varepsilon} - \bar{\mathbf{p}}\cdot\delta\bar{\mathbf{u}}_0)\,dA - \int_{(\Gamma_\sigma)} \bar{\mathbf{t}}\cdot\delta\bar{\mathbf{u}}_0\,ds \\ &+ \sum_{e=1}^{numel}\sum_{i=1}^{NGP}\frac{1}{A_i}\int_{\Omega_i}\int_{h^-}^{h^+} \mathbf{S}:\delta\mathbf{E}\;\bar{\mu}\;dz\;dA = 0\,. \end{aligned} \tag{15}$$

For the finite element formulation of the next section we need to derive the linearization of eq. (15). With conservative loads $\bar{\mathbf{p}}$ and $\bar{\mathbf{t}}$ one obtains

$$L\,[g(\mathbf{v},\delta\mathbf{v}), \Delta\mathbf{v}] := g(\mathbf{v},\delta\mathbf{v}) + Dg\cdot\Delta\mathbf{v} \tag{16}$$

where $g(\mathbf{v},\delta\mathbf{v})$ is given in (15) and

$$Dg\cdot\Delta\mathbf{v} = \int_{\Omega}(\Delta\boldsymbol{\sigma}\cdot\delta\boldsymbol{\varepsilon} + \boldsymbol{\sigma}\cdot\Delta\delta\boldsymbol{\varepsilon})\,dA + \sum_{e=1}^{numel}\sum_{i=1}^{NGP}\frac{1}{A_i}\int_{\Omega_i}\int_{h^-}^{h^+}(\Delta\mathbf{S}:\delta\mathbf{E} + \mathbf{S}:\Delta\delta\mathbf{E})\;\bar{\mu}\;dz\;dA \tag{17}$$

with $\Delta\boldsymbol{\sigma} = \mathbf{D}\;\Delta\boldsymbol{\varepsilon}$, $\Delta\mathbf{S} = \mathbf{C}\;\Delta\mathbf{E}$ and $\Delta\delta\mathbf{E} = \frac{1}{2}(\delta\mathbf{F}^T\Delta\mathbf{F} + \Delta\mathbf{F}^T\delta\mathbf{F})$. The material matrix $\mathbf{C}$ is a standard output of a library of constitutive laws in a material description. The linearized virtual shell strains $\Delta\delta\boldsymbol{\varepsilon}$ are derived for finite rotations in [30]. The stress resultant vector $\boldsymbol{\sigma}$ and the matrix of linearized stress resultants $\mathbf{D}$ are specified in the next section.

3 Finite element formulation

We describe a finite element formulation based on a standard displacement method. In the examples in section 5, also mixed elements are partly used. Concerning mixed hybrid element formulations for layered shells and solid shells we refer to [32], [4, 5].

The reference surface of the shell is discretized with *numel* quadrilateral isoparametric shell elements

$$\Omega^h = \sum_{e=1}^{numel} \Omega_e \,, \tag{18}$$

where the subscript h refers to the finite element approximation. Initial geometry, displacements and rotations are interpolated with bilinear functions $N_I(\xi,\eta) = \frac{1}{4}(1+\xi_I\,\xi)(1+\eta_I\,\eta)$ which are arranged in the matrix $\mathbf{N} = [N_1\mathbf{1}, N_2\mathbf{1}, N_3\mathbf{1}, N_4\mathbf{1}]^T$. Here, ξ,η are the coordinates in parameter space and $\xi_I = \pm 1, \eta_I = \pm 1$. The nodal degrees of freedom are three displacements and two or three rotations. At nodes with shell intersections three global rotations are present, whereas at the other nodes two local rotations are used. With incorporation of an assumed shear strain interpolation according to [33] shear locking can be avoided.
Inserting the interpolation functions for the displacements and virtual displacements into the linearized weak form (16) considering (15) and (17) yields

$$L\left[g(\mathbf{v}^h,\delta\mathbf{v}^h),\Delta\mathbf{v}^h\right] =$$
$$\sum_{e=1}^{numel} \begin{bmatrix} \delta\mathbf{v}^G \\ \delta\mathbf{V}_1 \\ \vdots \\ \delta\mathbf{V}_i \\ \vdots \\ \delta\mathbf{V}_{NGP} \end{bmatrix}_e^T \left\{ \begin{bmatrix} \mathbf{k}^G & \mathbf{0} & \vdots & \mathbf{0} & \vdots & \mathbf{0} \\ \mathbf{0} & \mathbf{K}_1^L & \vdots & \mathbf{0} & \vdots & \mathbf{0} \\ \dots & \dots & \ddots & \mathbf{0} & \dots & \dots \\ \mathbf{0} & \mathbf{0} & \mathbf{0} & \mathbf{K}_i^L & \mathbf{0} & \mathbf{0} \\ \dots & \dots & \dots & \mathbf{0} & \ddots & \dots \\ \mathbf{0} & \mathbf{0} & \dots & \mathbf{0} & \dots & \mathbf{K}_{NGP}^L \end{bmatrix}_e \begin{bmatrix} \Delta\mathbf{v}^G \\ \Delta\mathbf{V}_1 \\ \vdots \\ \Delta\mathbf{V}_i \\ \vdots \\ \Delta\mathbf{V}_{NGP} \end{bmatrix}_e + \begin{bmatrix} \mathbf{f}^G(\boldsymbol{\sigma}_i) \\ \mathbf{F}_1^L \\ \vdots \\ \mathbf{F}_i^L \\ \vdots \\ \mathbf{F}_{NGP}^L \end{bmatrix} \right\}_e \tag{19}$$

The indices G and L refer to the global and local boundary value problems, respectively. The matrices of the first row in (19) follow from the global part of the linearized weak form. The element residual vector and the tangential element stiffness matrix read

$$\mathbf{f}^G(\boldsymbol{\sigma}_i) = \int_{(\Omega_e)} (\mathbf{B}^T\boldsymbol{\sigma} - \mathbf{N}^T\bar{\mathbf{p}})\, dA - \int_{(\Gamma_{\sigma e})} \mathbf{N}^T\bar{\mathbf{t}}\, ds \qquad \mathbf{k}^G(\mathbf{D}_i) = \int_{(\Omega_e)} (\mathbf{B}^T\mathbf{D}\,\mathbf{B} + \mathbf{G})\, dA \tag{20}$$

where the matrices $\mathbf{B}$ and $\mathbf{G}$ are derived in [30]. The vector of stress resultants $\boldsymbol{\sigma}_i$ and linearized stress resultants $\mathbf{D}_i$ are specified below.
The matrices of the second to the last row in (19) are associated with the local boundary value problems at Gauss points $1 \le i \le NGP$ of shell element e. We continue with the local boundary value problem of Gauss point i with boundary conditions which are specified in the next section

$$\delta\mathbf{V}_i^T\left(\mathbf{K}_i^L\,\Delta\mathbf{V}_i + \mathbf{F}_i^L\right) = \frac{1}{A_i}\sum_{e=1}^{N} \delta\mathbf{v}_e^T(\mathbf{k}_e^L\,\Delta\mathbf{v}_e + \mathbf{f}_e^L)\,. \tag{21}$$

Here, the total number of elements used for the discretization of the RVE is denoted by N. The element residual vector $\mathbf{f}_e^L$ and the tangential element stiffness matrix $\mathbf{k}_e^L$ read

$$\mathbf{f}_e^L = \int_{(V_e)} \tilde{\mathbf{B}}^T\mathbf{S}\, dV \qquad \mathbf{k}_e^L = \int_{(V_e)} (\tilde{\mathbf{B}}^T\mathbf{C}\,\tilde{\mathbf{B}} + \tilde{\mathbf{G}})\, dV\,. \tag{22}$$

where $\tilde{\mathbf{B}}$ and $\tilde{\mathbf{G}}$ are the virtual strain displacement matrix and the geometrical matrix of 8–noded or 27–noded brick elements with standard displacement interpolation, respectively. For an effective finite element implementation a transformation of the Second Piola–Kirchhoff stress tensor $\mathbf{S}$ to the Kirchhoff stress tensor $\boldsymbol{\tau} = \mathbf{F}\mathbf{S}\mathbf{F}^T$ and of the material matrix $\mathbf{C}$ to the spatial form $\mathbf{c}$ is necessary. The integration is performed as in (22) with respect to the initial configuration. Hence one can take advantage of the fact that the spatial version of $\tilde{\mathbf{B}}$ is not fully populated which leads to a fast stiffness computation, see e.g. [31].

The element displacement vector $\mathbf{v}_e$ is now split in a part $\mathbf{v}_a$ which contains the internal displacements and a part $\mathbf{v}_b$ which contains the boundary displacements of the RVE. For elements which do not have boundary nodes $\mathbf{v}_b$ is not present. The relation of the internal displacements $\mathbf{v}_a$ to the global displacement vector $\mathbf{V}_i$ can be expressed using the standard assembly matrix $\mathbf{a}_e$. The relation of the boundary displacements $\mathbf{v}_b$ to the prescribed global shell strains $\boldsymbol{\varepsilon}_i$ at Gauss point i is given through a matrix $\mathbf{A}_e(x, y, z)$ which is specified in the next section. Thus we have

$$\mathbf{v}_e = \begin{bmatrix} \mathbf{v}_a \\ \mathbf{v}_b \end{bmatrix} = \begin{bmatrix} \mathbf{a}_e\, \mathbf{V}_i \\ \mathbf{A}_e\, \boldsymbol{\varepsilon}_i \end{bmatrix}. \tag{23}$$

The associated variations and linearizations are written as follows

$$\begin{bmatrix} \delta\mathbf{v}_a \\ \delta\mathbf{v}_b \end{bmatrix} = \begin{bmatrix} \mathbf{a}_e & \mathbf{0} \\ \mathbf{0} & \mathbf{A}_e \end{bmatrix} \begin{bmatrix} \delta\mathbf{V}_i \\ \delta\boldsymbol{\varepsilon}_i \end{bmatrix} \qquad \begin{bmatrix} \Delta\mathbf{v}_a \\ \Delta\mathbf{v}_b \end{bmatrix} = \begin{bmatrix} \mathbf{a}_e & \mathbf{0} \\ \mathbf{0} & \mathbf{A}_e \end{bmatrix} \begin{bmatrix} \Delta\mathbf{V}_i \\ \Delta\boldsymbol{\varepsilon}_i \end{bmatrix} \tag{24}$$

Introducing $\mathbf{k}_{\alpha\beta}$ and $\mathbf{f}_\alpha$ with $\alpha, \beta = a, b$ as submatrices of $\mathbf{k}_e^L$ and $\mathbf{f}_e^L$ in (21) leads to

$$\delta\mathbf{V}_i^T \left(\mathbf{K}_i^L\, \Delta\mathbf{V}_i + \mathbf{F}_i^L\right) = \frac{1}{A_i} \sum_{e=1}^{N} \begin{bmatrix} \delta\mathbf{v}_a \\ \delta\mathbf{v}_b \end{bmatrix}_e^T \left\{ \begin{bmatrix} \mathbf{k}_{aa} & \mathbf{k}_{ab} \\ \mathbf{k}_{ba} & \mathbf{k}_{bb} \end{bmatrix}_e \begin{bmatrix} \Delta\mathbf{v}_a \\ \Delta\mathbf{v}_b \end{bmatrix}_e + \begin{bmatrix} \mathbf{f}_a \\ \mathbf{f}_b \end{bmatrix}_e \right\} \tag{25}$$

and inserting (24) yields

$$\begin{aligned} & \delta\mathbf{V}_i^T \left(\mathbf{K}_i^L\, \Delta\mathbf{V}_i + \mathbf{F}_i^L\right) \\ = \; & \frac{1}{A_i} \sum_{e=1}^{N} \begin{bmatrix} \delta\mathbf{V}_i \\ \delta\boldsymbol{\varepsilon}_i \end{bmatrix}^T \left\{ \begin{bmatrix} \mathbf{a}_e^T\, \mathbf{k}_{aa}\, \mathbf{a}_e & \mathbf{a}_e^T\, \mathbf{k}_{ab}\, \mathbf{A}_e \\ \mathbf{A}_e^T\, \mathbf{k}_{ba}\, \mathbf{a}_e & \mathbf{A}_e^T\, \mathbf{k}_{bb}\, \mathbf{A}_e \end{bmatrix}_e \begin{bmatrix} \Delta\mathbf{V}_i \\ \Delta\boldsymbol{\varepsilon}_i \end{bmatrix} + \begin{bmatrix} \mathbf{a}_e^T\, \mathbf{f}_a \\ \mathbf{A}_e^T\, \mathbf{f}_b \end{bmatrix}_e \right\} \\ = \; & \frac{1}{A_i} \begin{bmatrix} \delta\mathbf{V}_i \\ \delta\boldsymbol{\varepsilon}_i \end{bmatrix}^T \left\{ \begin{bmatrix} \mathbf{K} & \mathbf{L} \\ \mathbf{L}^T & \mathbf{M} \end{bmatrix} \begin{bmatrix} \Delta\mathbf{V}_i \\ \Delta\boldsymbol{\varepsilon}_i \end{bmatrix} + \begin{bmatrix} \mathbf{F}_a \\ \mathbf{F}_b \end{bmatrix} \right\}. \end{aligned} \tag{26}$$

To alleviate the notation the Gauss point index i is omitted in the following matrices

$$\begin{aligned} \mathbf{K} &= \sum_{e=1}^{N} \mathbf{a}_e^T\, \mathbf{k}_{aa}\, \mathbf{a}_e & \mathbf{F}_a &= \sum_{e=1}^{N} \mathbf{a}_e^T\, \mathbf{f}_a \\ \mathbf{L} &= \sum_{e=1}^{N} \mathbf{a}_e^T\, \mathbf{k}_{ab}\, \mathbf{A}_e & \mathbf{F}_b &= \sum_{e=1}^{N} \mathbf{A}_e^T\, \mathbf{f}_b \\ \mathbf{M} &= \sum_{e=1}^{N} \mathbf{A}_e^T\, \mathbf{k}_{bb}\, \mathbf{A}_e\,. \end{aligned} \tag{27}$$

With $\delta\mathbf{V}_i \neq \mathbf{0}$ the internal degrees of freedom $\Delta\mathbf{V}_i$ can be eliminated from the set of equations using

$$\mathbf{K}\,\Delta\mathbf{V}_i + \mathbf{L}\,\Delta\boldsymbol{\varepsilon}_i + \mathbf{F}_a = \mathbf{0} \tag{28}$$

which yields

$$\Delta\mathbf{V}_i = -\mathbf{K}^{-1}\left(\mathbf{F}_a + \mathbf{L}\,\Delta\boldsymbol{\varepsilon}_i\right). \tag{29}$$

The inverse of $\mathbf{K}$ exists since rigid body motions are eliminated by boundary conditions. With (28) and (29) eq. (26) reduces to

$$\begin{aligned} \delta\mathbf{V}_i^T\left(\mathbf{K}_i^L\,\Delta\mathbf{V}_i + \mathbf{F}_i^L\right) &= \frac{1}{A_i}\delta\boldsymbol{\varepsilon}_i^T\left[\left(\mathbf{M} - \mathbf{L}^T\,\mathbf{K}^{-1}\,\mathbf{L}\right)\Delta\boldsymbol{\varepsilon}_i + \left(\mathbf{F}_b - \mathbf{L}^T\,\mathbf{K}^{-1}\,\mathbf{F}_a\right)\right] \\ &= \delta\boldsymbol{\varepsilon}_i^T(\mathbf{D}_i\,\Delta\boldsymbol{\varepsilon}_i + \boldsymbol{\sigma}_i) \end{aligned} \tag{30}$$

where

$$\boldsymbol{\sigma}_i = \frac{1}{A_i}(\mathbf{F}_b - \mathbf{L}^T\,\mathbf{K}^{-1}\,\mathbf{F}_a) \qquad\qquad \mathbf{D}_i = \frac{1}{A_i}(\mathbf{M} - \mathbf{L}^T\,\mathbf{K}^{-1}\,\mathbf{L}) \tag{31}$$

are the stress resultants and linearized stress resultants of Gauss point i. Finally (30) is inserted into the linearized coupled global-local boundary value problem (19)

$$L\left[g(\mathbf{v}^h, \delta\mathbf{v}^h), \Delta\mathbf{v}^h\right] =$$

$$\sum_{e=1}^{numel} \begin{bmatrix} \delta\mathbf{v}^G \\ \delta\boldsymbol{\varepsilon}_1 \\ \vdots \\ \delta\boldsymbol{\varepsilon}_i \\ \vdots \\ \delta\boldsymbol{\varepsilon}_{NGP} \end{bmatrix}_e^T \left\{ \begin{bmatrix} \mathbf{k}^G(\mathbf{D}_i) & \mathbf{0} & \vdots & \mathbf{0} & \vdots & \mathbf{0} \\ \mathbf{0} & \mathbf{D}_1 & \vdots & \mathbf{0} & \vdots & \mathbf{0} \\ \dots & \dots & \ddots & \mathbf{0} & \dots & \dots \\ \mathbf{0} & \mathbf{0} & \mathbf{0} & \mathbf{D}_i & \mathbf{0} & \mathbf{0} \\ \dots & \dots & \dots & \mathbf{0} & \ddots & \dots \\ \mathbf{0} & \mathbf{0} & \dots & \mathbf{0} & \dots & \mathbf{D}_{NGP} \end{bmatrix}_e \begin{bmatrix} \Delta\mathbf{v}^G \\ \Delta\boldsymbol{\varepsilon}_1 \\ \vdots \\ \Delta\boldsymbol{\varepsilon}_i \\ \vdots \\ \Delta\boldsymbol{\varepsilon}_{NGP} \end{bmatrix}_e + \begin{bmatrix} \mathbf{f}^G(\boldsymbol{\sigma}_i) \\ \boldsymbol{\sigma}_1 \\ \vdots \\ \boldsymbol{\sigma}_i \\ \vdots \\ \boldsymbol{\sigma}_{NGP} \end{bmatrix} \right\}_e \tag{32}$$

As eq. (32) shows there is coupling between the global and local problems. The shell strains $\boldsymbol{\varepsilon}_i$ enter in eq. (23), the stress resultants $\boldsymbol{\sigma}_i$ and the linearized stress resultants $\mathbf{D}_i$ according to (31) enter in $\mathbf{f}^G(\boldsymbol{\sigma}_i)$ and $\mathbf{k}^G(\mathbf{D}_i)$, respectively. The coupled nonlinear system of equations is simultaneously solved within a Newton iteration scheme. The iteration is terminated for the actual load step when local equilibrium in all Gauss points is attained along with the global equilibrium of the shell which is formulated through the first row of (19) or (32).

4 Boundary conditions of the RVE

In this section the boundary conditions for the RVE are specified. The so-called Hill condition [34] requires the equivalence of the microscopic and macroscopic stress power. With application of the Gauss theorem an alternative representation in terms of a surface integral can be derived, which shows that stress boundary conditions, displacement boundary conditions and periodic boundary conditions are conform with the Hill condition, e.g. [17].
A typical discretization of the RVE with applied boundary conditions is shown in Fig. 2. The coordinates of the RVE are bounded by

$$-l_x/2 \leq x \leq l_x/2 \quad , \quad -l_y/2 \leq y \leq l_y/2 \quad , \quad h^- \leq z \leq h^+ . \tag{33}$$

At the lower surface $z = h^-$ and at the upper surface $z = h^+$ stress boundary conditions, whereas at the lateral surfaces displacement boundary conditions are applied.
Assuming small strains the relation of the boundary displacements to the averaged strains $\bar{\mathbf{E}}$ is written as

$$\begin{bmatrix} \bar{u}_x \\ \bar{u}_y \\ \bar{u}_z \end{bmatrix} = \begin{bmatrix} \bar{E}_{11} & \bar{E}_{12} & \bar{E}_{13} \\ \bar{E}_{21} & \bar{E}_{22} & \bar{E}_{23} \\ \bar{E}_{31} & \bar{E}_{32} & \bar{E}_{33} \end{bmatrix} \begin{bmatrix} x \\ y \\ z \end{bmatrix}. \tag{34}$$

Inserting the relation of the averaged strains to the shell strains

$$\begin{aligned} \bar{E}_{11} &= \varepsilon_{11} + z\,\kappa_{11} \\ \bar{E}_{22} &= \varepsilon_{22} + z\,\kappa_{22} \\ \bar{E}_{33} &= 0 \\ \bar{E}_{12} &= \bar{E}_{21} = \varepsilon_{12} + z\,\kappa_{12} \\ 2\,\bar{E}_{13} &= 2\,\bar{E}_{31} = 2\,\varepsilon_{13} = \gamma_1 \\ 2\,\bar{E}_{23} &= 2\,\bar{E}_{32} = 2\,\varepsilon_{23} = \gamma_2 \end{aligned} \tag{35}$$

into (34) yields

$$\begin{bmatrix} \bar{u}_x \\ \bar{u}_y \\ \bar{u}_z \end{bmatrix} = \begin{bmatrix} \varepsilon_{11} + z\kappa_{11} & \varepsilon_{12} + z\kappa_{12} & \varepsilon_{13} \\ \varepsilon_{12} + z\kappa_{12} & \varepsilon_{22} + z\kappa_{22} & \varepsilon_{23} \\ \varepsilon_{13} & \varepsilon_{23} & 0 \end{bmatrix} \begin{bmatrix} x \\ y \\ z \end{bmatrix} \tag{36}$$

As is shown in the next section by means of a homogeneous RVE, these boundary conditions

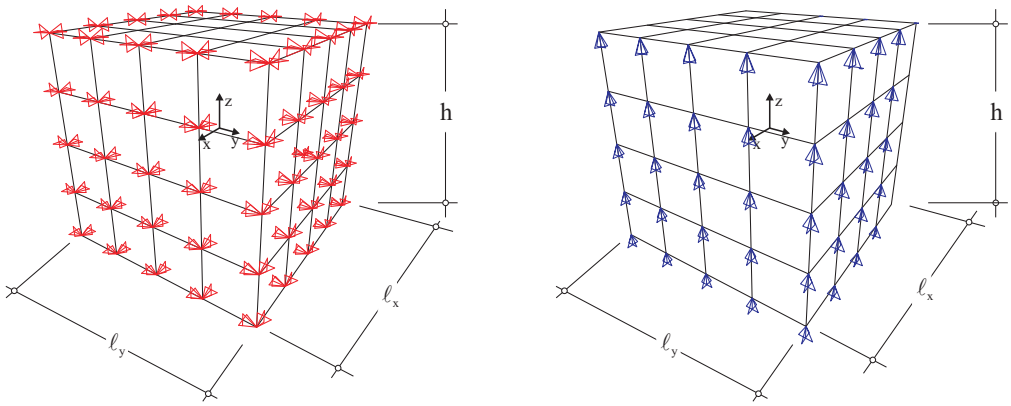

Figure 2: Boundary conditions on the RVE, left: fixed dofs, right: linked dofs.

exhibit severe restraints especially for particular membrane and bending modes. The reason is the constraint for the displacements $\bar{u}_z(x, y, \varepsilon_{13}, \varepsilon_{23})$. Therefore eq. (36) is modified such that boundary displacements $\bar{u}_z$ are not applied

$$\begin{bmatrix} \bar{u}_x \\ \bar{u}_y \end{bmatrix} = \begin{bmatrix} \varepsilon_{11} + z\kappa_{11} & \varepsilon_{12} + z\kappa_{12} & 2\,\varepsilon_{13} \\ \varepsilon_{12} + z\kappa_{12} & \varepsilon_{22} + z\kappa_{22} & 2\,\varepsilon_{23} \end{bmatrix} \begin{bmatrix} x \\ y \\ z \end{bmatrix} \tag{37}$$

Note that for the linear case (36) and (37) lead to the same transverse shear strains γ_α. Eq.

Table 1: Boundary conditions and link conditions

Nodes I on	prescribed displacements	link conditions
Faces: $x = -l_x/2,\ x = l_x/2$	$\bar{\mathbf{u}}_I = \mathbf{A}_I(x,y,z)\,\boldsymbol{\varepsilon}$	$u_z(l_x/2, y, z) = u_z(-l_x/2, -y, z)$
Faces: $y = -l_y/2,\ y = l_y/2$	$\bar{\mathbf{u}}_I = \mathbf{A}_I(x,y,z)\,\boldsymbol{\varepsilon}$	$u_z(x, l_y/2, z) = u_z(-x, -l_y/2, z)$

(37) is now rewritten with the vector of shell strains (2) as

$$\begin{bmatrix} \bar{u}_x \\ \bar{u}_y \end{bmatrix} = \begin{bmatrix} x & 0 & \frac{1}{2}y & xz & 0 & \frac{1}{2}yz & z & 0 \\ 0 & y & \frac{1}{2}x & 0 & yz & \frac{1}{2}xz & 0 & z \end{bmatrix} \begin{bmatrix} \varepsilon_{11} \\ \varepsilon_{22} \\ 2\varepsilon_{12} \\ \kappa_{11} \\ \kappa_{22} \\ 2\kappa_{12} \\ \gamma_1 \\ \gamma_2 \end{bmatrix} \tag{38}$$

$$\bar{\mathbf{u}}_I = \mathbf{A}_I(x,y,z)\,\boldsymbol{\varepsilon}\,,$$

where the index refers to node I of the considered element e. The matrices $\mathbf{A}_I$ are submatrices of $\mathbf{A}_e$ introduced in (23)

$$\mathbf{A}_e = \begin{bmatrix} \delta_1\,\mathbf{A}_1 \\ \vdots \\ \delta_I\,\mathbf{A}_I \\ \vdots \\ \delta_{nel}\,\mathbf{A}_{nel} \end{bmatrix}_{(2\,nel \times 8)} \qquad \delta_I = \begin{cases} 1 & \text{if node } I \text{ has fixed dofs} \\ 0 & \text{else} \end{cases} \tag{39}$$

The number of nodes nel is 8 or 27 for 8–noded or 27–noded elements, respectively.
Applying transverse shear strains γ_α via (38) to the RVE yields rigid body rotations and not shearing. The rigid body rotations can be avoided by further link conditions for the out of plane displacements. The comparison of two conditions in the next section shows that the out of plane displacements of nodes with same coordinates z on two opposite surfaces have to be linked with respect to the coordinates x and y in an antisymmetric way.
The applied boundary conditions and link conditions for the RVE are summarized in Table 1. Additionally, an arbitrary node is fixed in z-direction to avoid rigid body movements. When using an even number of elements we take the center node.

5 Examples

The developed model is implemented in a 5/6-parameter 4–node shell element within an extended version of the general finite element program FEAP [35]. With the first example we compare for a homogeneous RVE the finite element solutions with analytical expressions. The same is done with the next examples for a RVE with a cross-ply laminate and an angle-ply laminate. Furthermore, three coupled global local shell problems are investigated. Comparisons are given with full scale solutions computed with the solid shell elements [4, 5] and partially with standard shell solutions. The solid shell elements possess an orientation which

has to be considered when generating the mesh. For the present examples the thickness direction of the elements must coincide with the z–direction of the RVE. The element [4] is used here with assumed transverse shear strain interpolation (ANS) and 5 EAS parameters. The necessity of these options for optimal convergence is illustrated in Table 2. Using a mesh with one element the normalized bending terms D^b_{11} and D^b_{12} are computed. The solid shell element [5] is based on a Hu–Washizu variational formulation.

Table 2: Normalized bending stiffness parameters obtained with the solid shell element [4] using different options

ANS / EAS parameters	off / 0	on / 0	off / 5	on / 5
D^{bFE}_{11}/D^b_{11}	2.1	1.8	1.3	1.0
D^{bFE}_{12}/D^b_{12}	3.0	3.0	1.0	1.0

5.1 Homogeneous linear elastic isotropic RVE

In this example we consider a homogeneous RVE with $l_x = l_y = h = 2$ and linear elastic isotropic material behaviour. It is important to show that the developed homogenization method yields for this case the membrane, bending and shear stiffness of the Reissner–Mindlin shell theory

$$\begin{aligned} \mathbf{D} &= \int_{h^-}^{h^+} \mathbf{A}^T \mathbf{C}\, \mathbf{A}\, dz \qquad \mathbf{A} = \begin{bmatrix} \mathbf{1}_3 & z\mathbf{1}_3 & \mathbf{0} \\ \mathbf{0} & \mathbf{0} & \mathbf{1}_2 \end{bmatrix} \qquad \mathbf{C} = \begin{bmatrix} \mathbf{C}_m & \mathbf{0} \\ \mathbf{0} & \mathbf{C}_s \end{bmatrix} \\ \mathbf{D} &= \begin{bmatrix} \mathbf{D}^m & \mathbf{D}^{mb} & \mathbf{0} \\ \mathbf{D}^{mb} & \mathbf{D}^b & \mathbf{0} \\ \mathbf{0} & \mathbf{0} & \mathbf{D}^s \end{bmatrix} . \end{aligned} \tag{40}$$

The finite element solutions must display the correct structure of $\mathbf{D}$ with decoupling of the submatrices for membrane, bending and transverse shear. As an example, pure bending of a homogeneous shell would deliver besides the bending moments to membrane and shear forces, if the correct structure of $\mathbf{D}$ is not given.

5.1.1 Mid-surface as reference surface

Assuming linear elastic isotropy behaviour with elasticity data $E = 10^5$, $\nu = 0.4$ and shear modulus $G = \frac{E}{2(1+\nu)}$ yields

$$\mathbf{C}_m = \frac{E}{1-\nu^2} \begin{bmatrix} 1 & \nu & 0 \\ \nu & 1 & 0 \\ 0 & 0 & \frac{1-\nu}{2} \end{bmatrix} \qquad \mathbf{C}_s = G\, \mathbf{1}_2 \,. \tag{41}$$

With the mid-surface as reference surface, thus $h^- = -h/2$, $h^+ = h/2$, eq. (40) leads to the submatrices

$$\begin{aligned} \mathbf{D}^m &= h\,\mathbf{C}_m = \begin{bmatrix} D^m_{11} & D^m_{12} & 0 \\ D^m_{12} & D^m_{22} & 0 \\ 0 & 0 & D^m_{33} \end{bmatrix} \qquad \mathbf{D}^{mb} = \mathbf{0} \\ \mathbf{D}^b &= \frac{h^3}{12}\,\mathbf{C}_m = \begin{bmatrix} D^b_{11} & D^b_{12} & 0 \\ D^b_{12} & D^b_{22} & 0 \\ 0 & 0 & D^b_{33} \end{bmatrix} \qquad \mathbf{D}^s = \kappa\, h\, \mathbf{C}_s\,, \end{aligned} \tag{42}$$

where the shear correction factor κ is added on. Different definitions for κ are available in the literature, see [36] and references therein. As examples we mention the value $\kappa = 2/3$ of Timoshenko [37] and the result $\kappa = 5/6$ of Bach and Baumann [38] for rectangular beam cross sections.

The finite element solutions evaluating eq. $(31)_2$ yields exactly the zero entries in eq. (40) and (42) for arbitrary meshes starting with a $1 \times 1 \times 1$ discretization. The results for the non zero values are summarized for the different element formulations in Table 3. For the standard 8-node brick element mesh refinement is necessary to obtain convergence against the terms $D^b_{11} = D^b_{22}$ and D^b_{12}, see Fig. 3. The other element formulations lead to exact results for the membrane and bending terms. The exact values are obtained for all meshes starting with a $1 \times 1 \times 1$ discretization. Fig. 4 shows the convergence of κ using the different element formulations and the values for rectangular beam cross-sections of [38, 37].

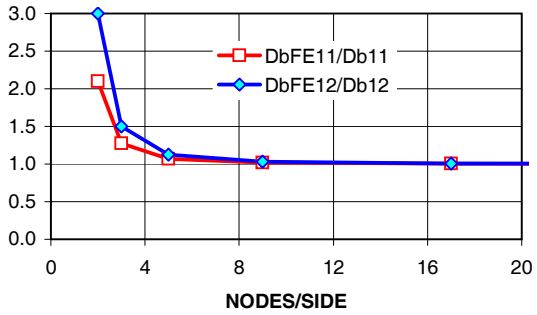

Figure 3: Normalized bending stiffness D^{bFE}_{11}/D^b_{11} and D^{bFE}_{12}/D^b_{12} for the 8-node brick element

Table 3: Results for the homogeneous linear elastic isotropic RVE

	8-node brick	27-node brick	solid shell [4]	solid shell [5]
$D^m_{11} = D^m_{22}$	exact	exact	exact	exact
D^m_{12}	exact	exact	exact	exact
D^m_{33}	exact	exact	exact	exact
$D^b_{11} = D^b_{22}$	Fig. 3	exact	exact	exact
D^b_{12}	Fig. 3	exact	exact	exact
D^b_{33}	exact	exact	exact	exact
κ	Fig. 4	Fig. 4	Fig. 4	Fig. 4

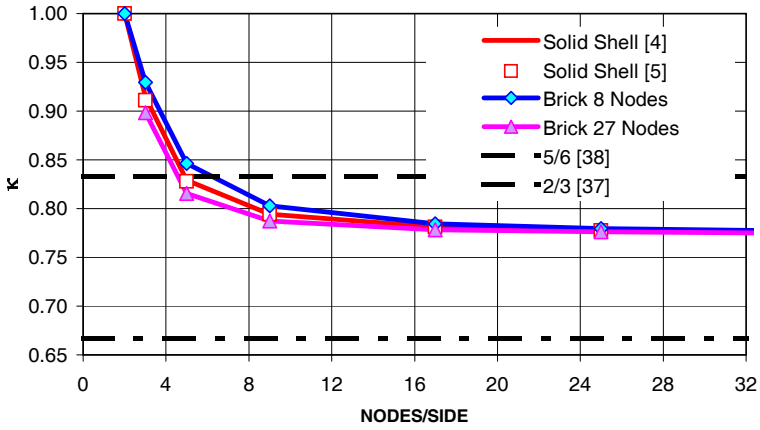

Figure 4: Shear correction factor versus nodes per side

5.1.2 Boundary conditions according to eq. (36)

We apply boundary conditions according to eq. (36) to the RVE. The zero entries in eq. (40) and (42) are obtained for arbitrary meshes starting with a $1 \times 1 \times 1$ discretization. The convergence of the non zero membrane and bending parameters is shown in Fig. 5. As can be seen $D^m_{11} = D^m_{22}, D^m_{12}, D^b_{11} = D^b_{22}, D^b_{33}$ converge against wrong values. The convergence of κ is comparable to Fig 4. This makes clear that displacement boundary conditions for the thickness direction exhibit severe restraints especially for particular membrane and bending modes.

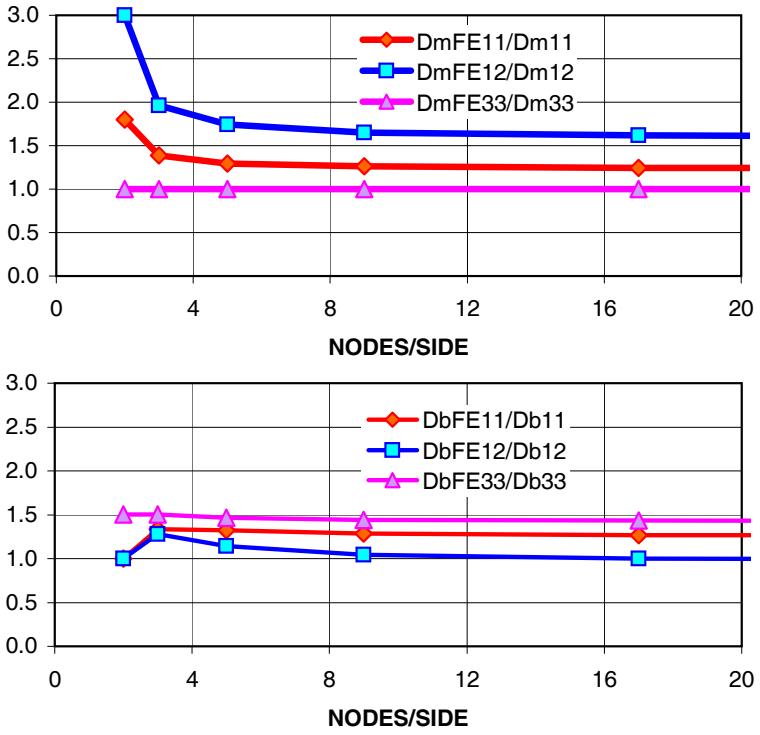

Figure 5: Convergence of some stiffness parameters for boundary conditions (36)

5.1.3 Comparison of two link conditions

In the following we investigate the influence of two different link conditions. We compare the link conditions of Table 1 with the conditions of eq. (43)

$$\begin{aligned} x = -l_x/2,\ x = l_x/2: &\qquad u_z(l_x/2, y, z) = u_z(-l_x/2, y, z) \\ y = -l_y/2,\ y = l_y/2: &\qquad u_z(x, l_y/2, z) = u_z(x, -l_y/2, z) \end{aligned} \tag{43}$$

where the z-displacements of nodes on two opposite surfaces are symmetrically linked together. As Fig. 6 shows, this yields a restraint to the warping deformations following from an applied torsion strain. As a consequence the torsional stiffness D_{33}^{bFE} converges with mesh refinement towards a wrong value, see Fig. 7. Again, solid shell [4] is used for the discretization. The same behaviour follows with the other element formulations. The comparison shows that the mechanical answer of the RVE behaves very sensitive to inappropriate constraints for the displacements in thickness direction of the shell.

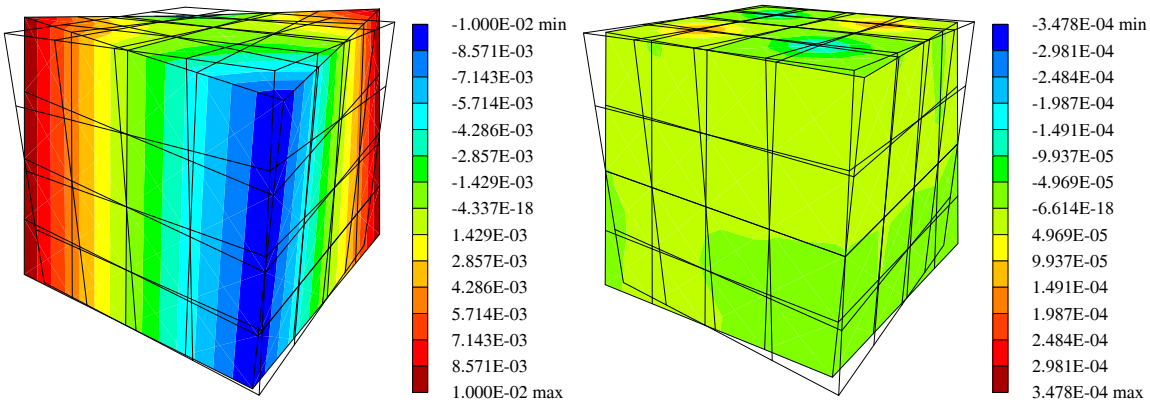

Figure 6: Mesh, deformed mesh (10 times amplified) and displacements u_z for a torsion strain $2\,\kappa_{12} = 0.02$, left: link conditions Table 1, right: link conditions eq. (43)

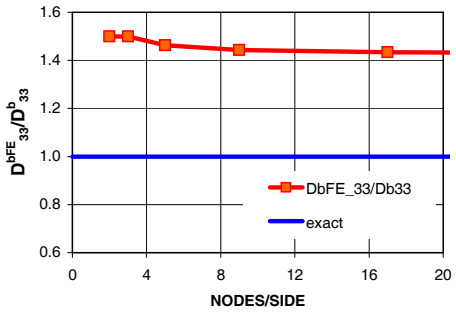

Figure 7: Convergence of the normalized torsional stiffness D_{33}^{bFE}/D_{33}^{b} for link conditions (43)

5.1.4 Bottom surface as reference surface

We choose a reference surface at the bottom of the RVE, thus $h^- = 0$ and $h^+ = h$. The submatrices of $\mathbf{D}$ according to (40) are given as follows. The membrane stiffness $\mathbf{D}^m$ and the

shear stiffness $\mathbf{D}^s$ remain unchanged, wheras the bending stiffness and the coupling matrix become

$$\mathbf{D}^b = \frac{h^3}{3}\mathbf{C}_m \qquad\qquad \mathbf{D}^{mb} = \frac{h^2}{2}\mathbf{C}_m\,, \tag{44}$$

respectively.
The finite element results correspond to Table 3. Again mesh refinement is necessary for the terms $D^b_{11} = D^b_{22}$ and D^b_{12} when using the standard 8-node brick element. The results are close to those depicted in Fig. 3. The results for the shear terms are identical with Fig. 4. The coupling matrix $\mathbf{D}^{mb}$ is exact for all element types and all meshes.

5.2 RVE with a cross-ply laminate

We consider a RVE with mid-surface as reference surface, $l_x = l_y = h = 2\,mm$ and a $[0°/90°/0°]$ cross-ply laminate. The layers are of equal thickness and $0°$ corresponds to the x-direction. The material constants for transversal isotropy are chosen as

$$\begin{aligned} E_1 &= 125000\,N/mm^2 & \qquad G_{12} &= 4800\,N/mm^2 \\ E_2 &= 7400\,N/mm^2 & \qquad G_{23} &= 2700\,N/mm^2 \\ \nu_{12} &= 0.34\,, \end{aligned} \tag{45}$$

where the index 1 refers to the preferred direction of the material. Hence, the matrices $\mathbf{C}_m$ and $\mathbf{C}_s$ of eq. (40) read with $\Delta = 1 - \nu_{12}^2\dfrac{E_2}{E_1}$

$$\mathbf{C}_m = \begin{bmatrix} E_1/\Delta & \nu_{12}E_2/\Delta & 0 \\ \nu_{12}E_2/\Delta & E_2/\Delta & 0 \\ 0 & 0 & G_{12} \end{bmatrix} \qquad\qquad \mathbf{C}_s = \begin{bmatrix} G_{12} & 0 \\ 0 & G_{23} \end{bmatrix}. \tag{46}$$

The evaluation of (40) considering (46) and the fibre angle in each layer yields a matrix $\mathbf{D}$ with the following submatrices

$$\begin{aligned} \mathbf{D}^m &= \frac{h}{3\,\Delta}\begin{bmatrix} 2\,E_1 + E_2 & 3\,\nu_{12}\,E_2 & 0 \\ 3\,\nu_{12}\,E_2 & E_1 + 2\,E_2 & 0 \\ 0 & 0 & 3\,\Delta\,G_{12} \end{bmatrix} \\ \mathbf{D}^b &= \frac{h^3}{324\,\Delta}\begin{bmatrix} 26\,E_1 + E_2 & 27\,\nu_{12}\,E_2 & 0 \\ 27\,\nu_{12}\,E_2 & E_1 + 26\,E_2 & 0 \\ 0 & 0 & 27\,\Delta\,G_{12} \end{bmatrix} \\ \mathbf{D}^{mb} &= \mathbf{0} \\ \mathbf{D}^s &= \frac{h}{3}\begin{bmatrix} \kappa_1(2\,G_{12} + G_{23}) & 0 \\ 0 & \kappa_2(G_{12} + 2\,G_{23}) \end{bmatrix}. \end{aligned} \tag{47}$$

As in the last example, we again compare the finite element results obtained by evaluation of $(31)_2$ with the values in (47). The zero entries in eq. (40) and (47) are exact for arbitrary meshes starting with a $1 \times 1 \times 1$ discretization for each layer. The results for the non zero values are summarized for the different element formulations in table 4. The normalized stiffness parameters D^b_{11}, D^b_{22} and D^b_{12} obtained with the 8-node brick element are depicted in

Fig. 8. The other element formulations lead to exact results for the membrane and bending terms. The exact values are obtained for all meshes starting with a $1 \times 1 \times 1$ discretization for each layer. Fig. 9 shows the convergence of the two shear correction factors κ_1 and κ_2 using the different element formulations.

Table 4: Results for the RVE with a cross ply laminate [0°/90°/0°]

	8-node brick	27-node brick	solid shell [4]	solid shell [5]
D^m_{11}	exact	exact	exact	exact
D^m_{12}	exact	exact	exact	exact
D^m_{22}	exact	exact	exact	exact
D^m_{33}	exact	exact	exact	exact
D^b_{11}	Fig. 8	exact	exact	exact
D^b_{12}	Fig. 8	exact	exact	exact
D^b_{22}	Fig. 8	exact	exact	exact
D^b_{33}	exact	exact	exact	exact
κ_1, κ_2	Fig. 9	Fig. 9	Fig. 9	Fig. 9

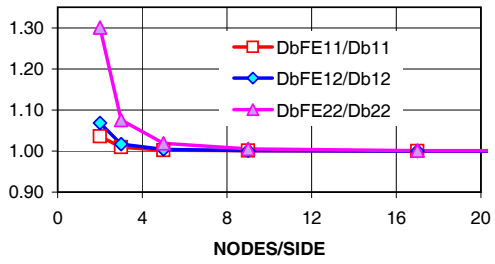

Figure 8: Normalized bending stiffness parameters versus nodes per side

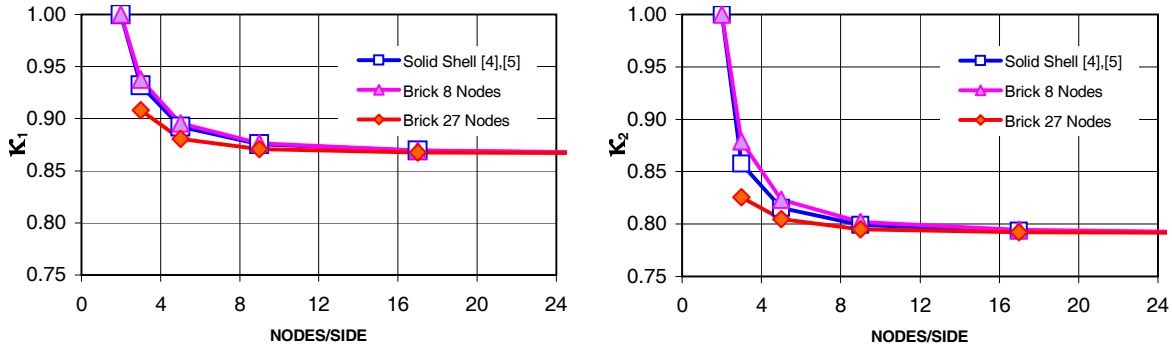

Figure 9: Shear correction factors versus nodes per side, left: κ_1, right: κ_2

5.3 RVE with an angle-ply laminate

We consider a RVE with mid-surface as reference surface, $l_x = l_y = h = 2\,mm$ and a $[-45°/45°]$ angle-ply laminate. The layers are of equal thickness and $0°$ corresponds to the x-direction. The material constants for transversal isotropy are given in (45). The evaluation of (40) considering (46) and the fibre angles in both layers yields a matrix $\mathbf{D}$ with the following submatrices

$$
\begin{aligned}
\mathbf{D}^m &= \frac{h}{4\,\Delta}\begin{bmatrix} D_{11} & D_{12} & 0 \\ D_{12} & D_{11} & 0 \\ 0 & 0 & D_{33} \end{bmatrix} && D_{11} = E_1 + (1+2\nu_{12})E_2 + 4\,\Delta\,G_{12} \\
& && D_{12} = E_1 + (1+2\nu_{12})E_2 - 4\,\Delta\,G_{12} \\
& && D_{33} = E_1 + (1-2\nu_{12})E_2 \\
\mathbf{D}^b &= \frac{h^3}{48\,\Delta}\begin{bmatrix} D_{11} & D_{12} & 0 \\ D_{12} & D_{11} & 0 \\ 0 & 0 & D_{33} \end{bmatrix} \\
\mathbf{D}^{mb} &= \frac{h^2}{16\,\Delta}\begin{bmatrix} 0 & 0 & D_{13} \\ 0 & 0 & D_{13} \\ D_{13} & D_{13} & 0 \end{bmatrix} && D_{13} = E_1 - E_2 \\
\mathbf{D}^s &= \frac{h}{2}\begin{bmatrix} \kappa(G_{12}+G_{23}) & 0 \\ 0 & \kappa(G_{12}+G_{23}) \end{bmatrix}.
\end{aligned}
\tag{48}
$$

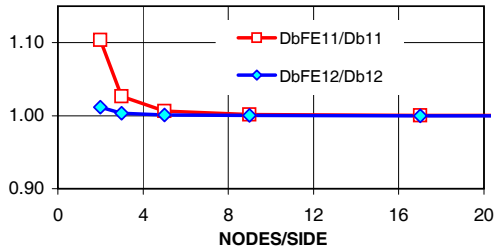

Figure 10: Normalized bending stiffness parameters versus nodes per side

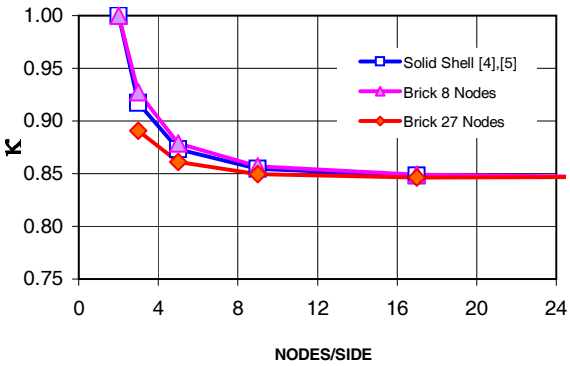

Figure 11: Shear correction factor versus nodes per side

We again compare the finite element results obtained by evaluation of $(31)_2$ with (48). The zero entries in eq. (40) and (48) are exact for arbitrary meshes starting with a $1 \times 1 \times 1$

discretization for each layer. The results for the non zero values are summarized for the different element formulations in table 5. The normalized stiffness parameters $D^b_{11} = D^b_{22}$ and D^b_{12} obtained with the 8-node brick element are depicted in Fig. 10. The torsion stiffness D^b_{33} converges against the analytical result, where the coarsest mesh yields practically already the converged value. The other element formulations lead to exact results for the membrane terms, bending terms and coupling terms. The exact values are obtained for all meshes starting with a $1 \times 1 \times 1$ discretization for each layer. Fig. 11 shows the convergence of the shear correction factor κ.

Table 5: Results for the RVE with an angle-ply laminate $[-45°/45°]$

	8-node brick	27-node brick	solid shell [4]	solid shell [5]
$D^m_{11} = D^m_{22}$	exact	exact	exact	exact
D^m_{12}	exact	exact	exact	exact
D^m_{33}	exact	exact	exact	exact
$D^b_{11} = D^b_{22}$	Fig. 10	exact	exact	exact
D^b_{12}	Fig. 10	exact	exact	exact
D^{bFE}_{33}/D^b_{33}	≤ 1.00013	exact	exact	exact
D^{mb}_{13}	exact	exact	exact	exact
κ	Fig. 11	Fig. 11	Fig. 11	Fig. 11

5.4 Layered cylindrical panel subjected to a concentrated load

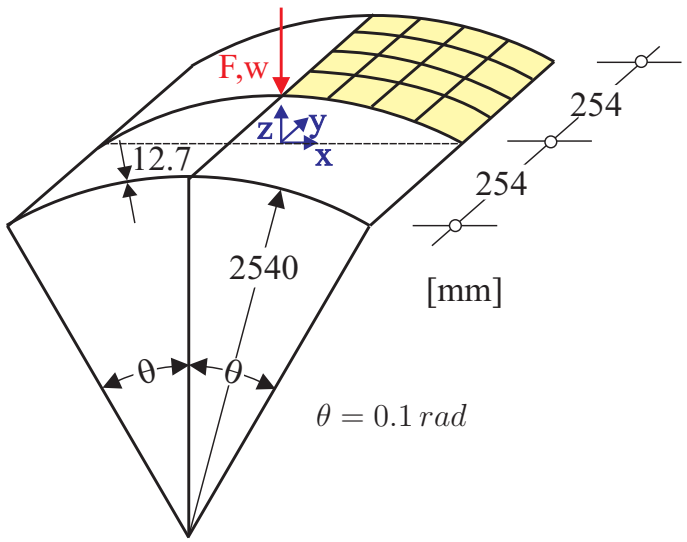

Material data:

$$\begin{aligned} E_1 &= 3300\, N/mm^2 \\ E_2 &= 1100\, N/mm^2 \\ G_{12} &= 660\, N/mm^2 \\ G_{23} &= 450\, N/mm^2 \\ \nu_{12} &= 0.30 \end{aligned}$$

Meshes:

Shell	4×4
Solid Shell	$4 \times 4 \times (4+4+4)$
RVE	$4 \times 4 \times (4+4+4)$

Figure 12: Cylindrical panel subjected to a concentrated load and material data

In this example we consider a layered cylindrical panel subjected to a concentrated load. The boundary conditions are as follows: soft support with $u_x = u_y = u_z = 0$ for the straight boundaries and stress free curved boundaries. Two layer sequences are considered: $[0°/90°/0°]$ and $[90°/0°/90°]$, where $0°$ refers to the circumferential direction and $90°$ to the length direction of the panel. Considering symmetry one quarter of the panel is discretized. The RVE and

the full scale model are discretized in thickness direction with four elements for each layer. The geometrical and material data for transversal isotropic material behaviour and the mesh densities are given in Fig. 12.

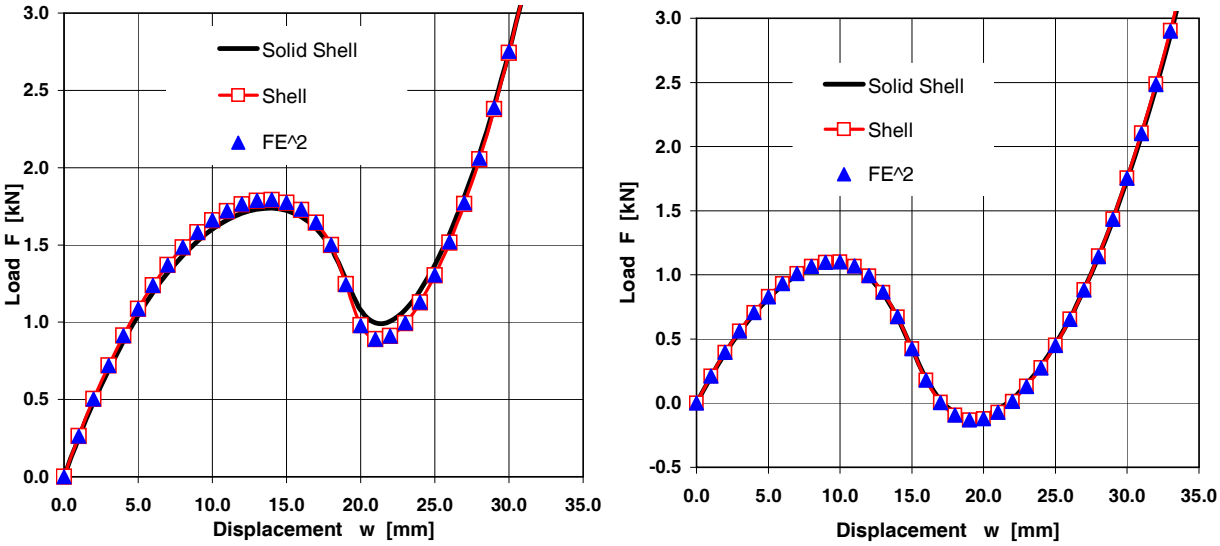

Figure 13: Load displacement curves for $[0°/90°/0°]$(left) and for $[90°/0°/90°]$(right)

All computations are carried out displacement controlled. The reactions F are computed for applied deflections w of the loading point using different models. We compare shell and solid shell solutions using the elements [32, 4, 5] with solutions of the two–scale model. For this example there is virtually no difference between a geometrically linear and nonlinear analysis of the RVE. As Fig. 13 shows the layer sequence $[0°/90°/0°]$ provides a stiffer behaviour. The computed curves of the different models are in good agreement with literature results, e.g. [39].

5.5 Layered cylindrical shell

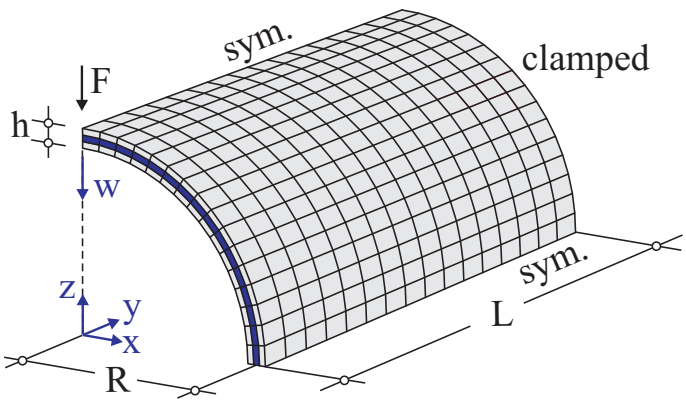

Geometrical data:

$$\begin{aligned} L &= 300 \quad mm \\ R &= 100 \quad mm \\ h &= 1 \quad mm \end{aligned}$$

Meshes:

Shell	16×16
Solid Shell	$16 \times 16 \times (4+4+4)$
RVE	$4 \times 4 \times (4+4+4)$

Figure 14: Layered cylindrical shell, geometrical data and mesh densities

Fig. 14 shows a quarter of a cylindrical fiber reinforced composite shell with boundary conditions, loading, geometrical data and mesh densities. The fiber angles for the three layers of equal thickness are [90°/0°/90°], where 0° refers to the circumferential direction and 90° to the length direction of the cylinder. The material data for transversal isotropic material behaviour are given in eq. (45).
The computations are carried out displacement controlled, thus F is computed as reaction for prescribed displacements w. We compare shell solutions and 3d full scale solutions using the elements [32, 4, 5] with results of the two–scale model. The RVE and the full scale model are discretized in thickness direction with four elements for each layer. Again there is virtually no difference between a geometrically linear and nonlinear computation of the RVE. The curves in Fig. 15 show good agreement between the different models. A plot of the deformed configuration is shown in Fig. 16. The largest deformations occur in the vicinity of the concentrated load.

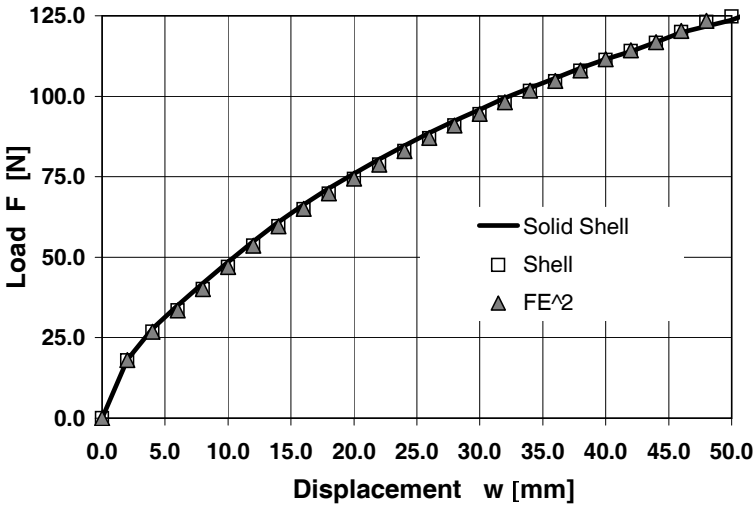

Figure 15: Load F versus displacement w for the layered shell

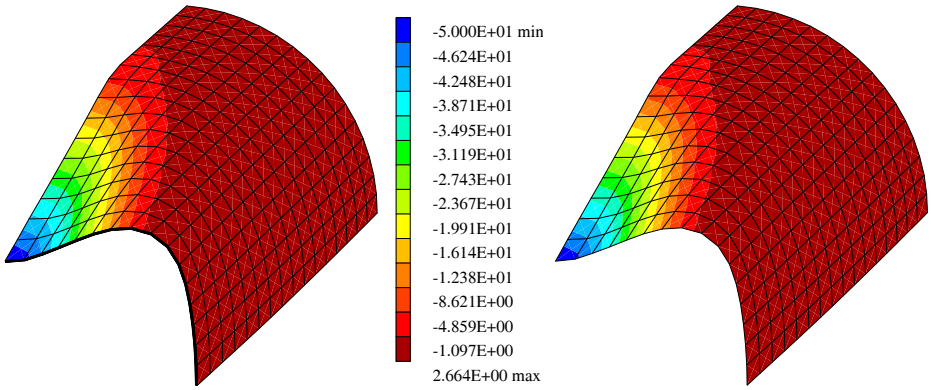

Figure 16: Final deformed configuration (left: solid shell, right: FE^2/shell)

This is the motivation for an adaptive modeling of the problem, see Fig. 17. To save computing time the two-scale computation is carried out only in the domain $0 \leq y \leq L/4$. The

remaining part of the structure is discretized with shell elements [32]. The results of the different models are plotted in Fig. 18.

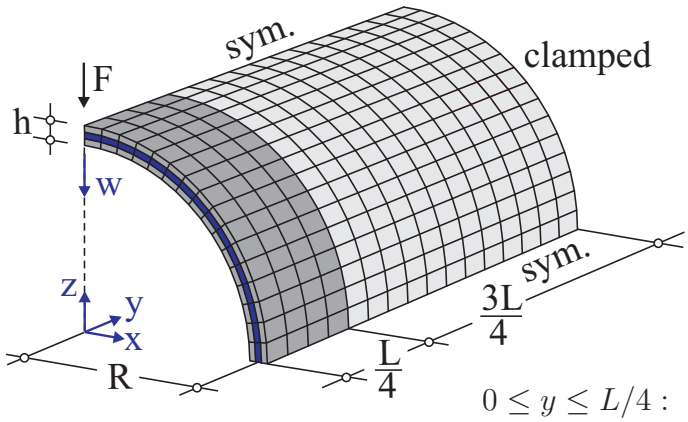

$0 \le y \le L/4:$ FE^2, 16×4 elements

$L/4 \le y \le L:$ Shell [32], 16×12 elements

Figure 17: Layered cylindrical shell with adaptive meshing

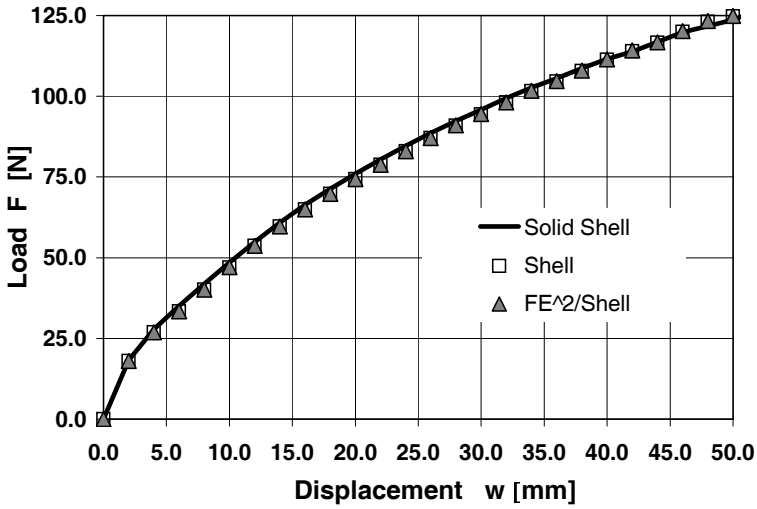

Figure 18: Load deflection curves for the adaptive computation

5.6 Sandwich plate strip

Fig. 19 shows a sandwich plate strip with coordinates x, y defined in the range $-L/2 \le x \le L/2$ and $-b/2 \le y \le b/2$, subjected to a constant load $q = \lambda \cdot 10^{-3} N/mm^2$. The plate consists of a core with thickness t_c and of outer face layers with thickness t_f. The structure is simply supported at $x = \pm L/2, z = 0$, and plane strain boundary conditions are assumed at $y = \pm b/2$. This example is characterized by geometrical and physical nonlinear behaviour of the RVE. The material data for isotropy are E_c, ν_c for the elastic core and E_f, ν_f for the elastic plastic face layers with yield stress y_0 and linear hardening ξ. Considering symmetry of the structure the number of elements in y-direction is 1 and in x-direction is $N = 5, 10, 20, 50$.

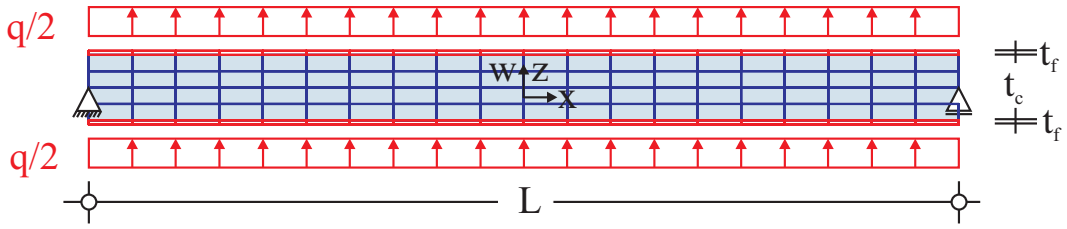

Geometrical data:

L	=	2000	mm
t_c	=	30	mm
t_f	=	0.5	mm
b	=	60	mm

Material data:

E_c	=	70	N/mm^2
ν_c	=	0.3	
E_f	=	70000	N/mm^2
ν_f	=	0.3	
y_0	=	100	N/mm^2
ξ	=	1000	N/mm^2

Meshes:

Shell	$N \times 1$
3D	$N \times 1 \times (10+2)$
RVE	$4 \times 4 \times (10+2)$

Figure 19: Sandwich plate strip (not to scale)

The RVE and the full scale model are discretized in thickness direction with 10 elements for the core and one element for each face layer. All data are summarized in Fig. 19.
The computations are carried out load controlled. The displacements w are computed for load factors $\lambda = 1.0, 2.0, 3.0, 3.2, ..., 5.0$ and for unloading with $\lambda = 5.0, 4.0, ..., 0.0$. The results of the two-scale model are compared with the 3d solution obtained with the solid shell element [4] in Fig. 20. The two-scale model yields with practically $N = 10$ elements a converged solution, whereas for the 3d full scale solution $N = 50$ elements are necessary for a converged solution. A plot of the deformed configuration at $\lambda = 5$ is shown in Fig. 21.
For $N = 5$ elements the convergence behaviour of the Newton scheme when applying the simultaneous iteration in comparison to a nested iteration is depicted in Table 6. Within the load steps $\lambda = 4.6$ and $\lambda = 4.8$ the norm of the global residual vector $|\mathbf{F}|$ is shown for each iteration. Both procedures show quadratic convergence and require the same number of iterations, however the nested iteration additionally needs 2 to 6 local iterations in each global iteration step. The number of local iterations is determined in the element closest to the symmetry line.

6 Conclusions

A coupled two-scale model for layered shells is developed and tested with several examples. The boundary conditions for the RVE are chosen in such a way that particular membrane, bending and shear modes are not restrained. This is shown by means of a homogeneous RVE, where a material matrix for the stress resultants with decoupled submatrices for membrane, bending and shear comes out. For the discretization of the RVE solid shell elements with assumed strain interpolation and enhanced strain interpolation are advantageous, since in comparison to standard 8-noded brick elements a better convergence behaviour is given. The

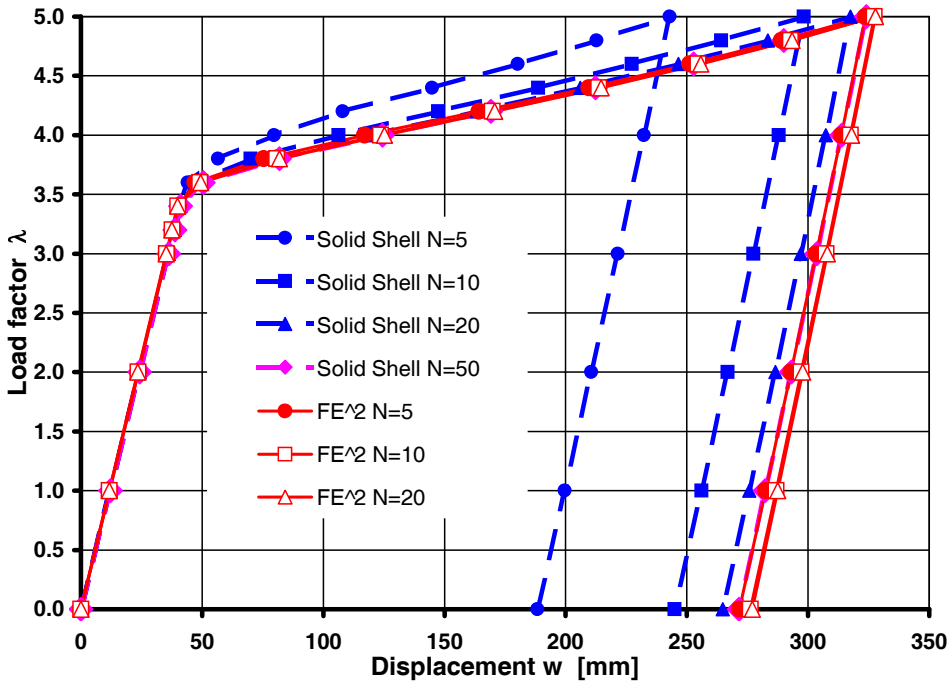

Figure 20: Load factor λ versus displacement w for the sandwich plate strip

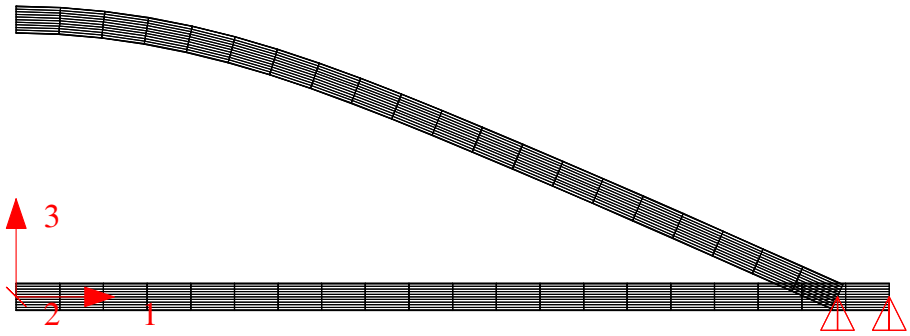

Figure 21: Deformed mesh of half the structure at $\lambda = 5$ (full scale solution, N=20)

systems of nonlinear equations for the coupled global and local boundary value problems are solved simultaneously within the Newton iteration scheme. This is numerically more effective than a nested iteration. The developed FE^2 method is well suited for an adaptive modeling of thin structures.

References

[1] Mittelstedt, C., Becker, W.: Interlaminar stress concentrations in layered structures, Part I: A selective literature survey on the free-edge effect since 1967, Journal of Composite Materials, **38**, 1037-1062, 2004.

[2] Reddy JN: Mechanics of Laminated Composite Plates and Shells: Theory and Analysis (2nd edn). CRC Press, London, 2004.

Table 6: Iteration behaviour for simultaneous and nested iteration

Load Step	Iteration	Simultaneous Iteration $\|\mathbf{F}\|$	Number of local Iterations	Nested Iteration $\|\mathbf{F}\|$	Number of local Iterations
$\lambda = 4.6$	1	3.50E-03	1	3.50E-03	6
	2	3.72E+00	1	4.98E+00	5
	3	4.52E+00	1	5.89E+00	4
	4	9.20E-02	1	4.09E-02	3
	5	8.16E-05	1	8.07E-06	3
	6	1.51E-06	1	1.72E-06	2
$\lambda = 4.8$	1	3.50E-03	1	3.50E-03	6
	2	2.40E+00	1	4.09E+00	5
	3	4.25E+00	1	5.68E+00	4
	4	8.05E-02	1	2.32E-02	3
	5	1.13E-04	1	5.17E-06	3
	6	8.68E-07	1	1.18E-06	2

[3] Gruttmann F., Wagner W.: Coupling of two– and three–dimensional composite shell elements in linear and nonlinear applications, Comp. Meth. Appl. Mech. Engrg., **129**, 271–287, 1996.

[4] Klinkel S., Gruttmann F., Wagner W.: A Continuum Based 3D–Shell Element for Laminated Structures, Computers & Structures, **71**, 43–62, 1999.

[5] Klinkel, S. Gruttmann, F. Wagner, W.: A robust non–linear solid shell element based on a mixed variational formulation, Comp. Meth. Appl. Mech. Engrg, **195**, 179-201, 2006.

[6] Hohe J, Becker W.: Effective stress–strain relations for two dimensional cellular sandwich cores: homogenization, material models, and properties, Applied Mechanics Reviews **55**, 61–87, 2002.

[7] Rabczuk T, Kim JY, Samaniego E, Belytschko T.: Homogenization of sandwich structures, Int. J. Num. Meth. Engng., **61**, 1009–1027, 2004.

[8] Liu T, Deng ZC, Lu TJ.: Design optimization of truss-cored sandwiches with homogenization. Int. J. Sol. Struct., **43**, 7891–7918, 2006.

[9] Cecchi A, Sab K.: Out-of-plane model for heterogeneous periodic materials: the case of masonry. European Journal of Mechanics A Solids **21**, 715–746, 2002.

[10] Cecchi A, Milani G, Tralli A.: A Reissner-Mindlin limit analysis model for out-of-plane loaded running bond masonry walls, Int. J. Sol. Struct., **44**, 1438–1460, 2007.

[11] Mistler M, Anthoine A, Butenweg C.: In-plane and out-of-plane homogenization of masonry, Computers and Structures, **85**, 1321–1330, 2007.

[12] Mercatoris B.C.N., Bouillard P, Massart T.J.: Multi-scale detection of failure in planar masonry thin shells using computational homogenization, Engineering Fracture Mechanics, **76**, 479–499, 2009.

[13] Mercatoris B.C.N., Massart T.J.: A coupled two–scale computational scheme for the failure of periodic quasi-brittle thin planar shells and its application to masonry, Int. J. Num. Meth. Engng., **85**, 1177–1206, 2011.

[14] Geers M.G.D., Coenen E.W.C., Kouznetsova V.G.: Multi–scale computational homogenization of structured thin sheets, Modelling Simul. Mater. Sci. Eng., **15**, S393-S404, 2007.

[15] Coenen E.W.C., Kouznetsova V.G., Geers M.G.D.: Computational homogenization for heterogeneous thin sheets, Int. J. Numer. Meth. Engng, **83**, 1180–1205, 2010.

[16] Helfen C., Diebels, S.: Numerical multiscale modelling of sandwich plates, Technische Mechanik, **32**, 2-5, 251– 264, 2012.

[17] Zohdi T.I., Wriggers P.: Introduction to Computational Micromechanics, Springer Series: Lecture Notes in Applied and Computational Mechanics **20**, Springer Berlin Heidelberg 2005.

[18] De Borst R., Ramm E.: Multiscale methods in computational mechanics: progress and accomplishments, Springer Series: Lecture Notes in Applied and Computational Mechanics **55**, Springer Berlin Heidelberg 2011.

[19] Guedes JM, Kikuchi N.: Preprocessing and postprocessing for materials based on the homogenization method with adaptive finite element methods. Comp. Meth. Appl. Mech. Engrg, **83**, 143–198, 1990.

[20] Ghosh S, Lee K, Moorthy S.: Two scale analysis of heterogeneous elastic-plastic materials with asymptotic homogenisation and Voronoi cell finite element model. Comp. Meth. Appl. Mech. Engrg, **132**, 63–116, 1996.

[21] Miehe C, Schröder J, Schotte J.: Computational homogenization analysis in finite plasticity, simulation of texture development in polycrystalline materials, Comp. Meth. Appl. Mech. Engrg, **171**, 387–418, 1999.

[22] Michel JC, Moulinec H, Suquet P.: Effective properties of composite materials with periodic microstructure: a computational approach, Comp. Meth. Appl. Mech. Engrg, **172**, 109–143, 1999.

[23] Feyel F, Chaboche JL.: FE2 multiscale approach for modelling the elastoviscoplastic behaviour of long fiber SiC/Ti composite materials, Comp. Meth. Appl. Mech. Engrg, **183**, 309—330, 2000.

[24] Terada K, Kikuchi N.: A class of general algorithms for multi-scale analysis of heterogeneous media, Comp. Meth. Appl. Mech. Engrg, **190**, 5427–5464, 2001.

[25] Ghosh S, Lee K, Raghavan P.: A multi-level computational model for multi-scale damage analysis in composite and porous materials. Int. J. Sol. Struct., **38**, 2335–2385, 2001.

[26] Kouznetsova V, Brekelmans WAM, Baaijens FPT: An approach to micro–macro modeling of heterogeneous materials, Computational Mechanics, **27**, 37–48, 2001.

[27] Miehe C, Koch A.: Computational micro-to-macro transition of discretized microstructures undergoing small strain, Archive of Applied Mechanics, **72**, 300–317, 2002.

[28] Oskay, C., Fish, J.: Eigendeformation-based reduced order homogenization for failure analysis of heterogeneous materials Comput. Methods Appl. Mech. Engrg. **196**, 1216–1243, 2007.

[29] Fish, J.: Multiscale Modeling and Simulation of Composite Materials and Structures, in: de Borst R., Ramm E.(eds.) Multiscale methods in computational mechanics: progress and accomplishments, Springer Series: Lecture Notes in Applied and Computational Mechanics **55**, 215-232, 2011. 2011.

[30] Wagner, W., Gruttmann, F.: A robust nonlinear mixed hybrid quadrilateral shell element, Int. J. Num. Meth. Engng., **64**, 635–666, 2005.

[31] Zienkiewicz OC, Taylor RL.: The Finite Element Method for Solid and Structural Mechanics, 6. ed., Elsevier Butterworth Heinemann: Oxford, 2005.

[32] Gruttmann, F., Wagner, W.: Structural analysis of composite laminates using a mixed hybrid shell element, Computational Mechanics, **37**, 479–497, 2006.

[33] Dvorkin E, Bathe KJ.: A continuum mechanics based four node shell element for general nonlinear analysis, Engineering Computations, **1**, 77–88, 1984.

[34] Hill R.: Elastic properties of reinforced solids: some theoretical principles, J. Mech. Phys. Solids, **11**, 357–372, 1963.

[35] Taylor RL, Feap User Manual, http://www.ce.berkeley.edu/projects/feap/manual.pdf

[36] Gruttmann F., Wagner W.: Shear correction factors in Timoshenko's beam theory for arbitrary cross-sections, Computational Mechanics, **27**, 199–207, 2001.

[37] Timoshenko, S. P. (1940): Strength of Materials, 2nd edn, D. Van Nostrand Company, Inc., New York.

[38] Bach C., Baumann R. (1924): Elastizität und Festigkeit, 9th edn, Springer, Berlin

[39] Saigal, S., Kapania, R. K., Yang, T. Y.: Geometrically Nonlinear Finite Element Analysis of imperfect Laminated Shells, J. Composite Materials **20**, 197–214, 1986.